ELSEVIER

J. Non-Newtonian Fluid Mech., 60 (1995) 129–154

Journal of Non-Newtonian Fluid Mechanics

# A boundary integral method for two-dimensional (non)-Newtonian drops in slow viscous flow

E.M. Toose [a,*], B.J. Geurts [b], J.G.M. Kuerten [b]

[a] *Department of Applied Physics, University of Twente, P.O. Box 217, 7500 AE Enschede, The Netherlands*

[b] *Department of Applied Mathematics, University of Twente, P.O. Box 217, 7500 AE Enschede, The Netherlands*

Received 22 January 1995; in revised form 20 July 1995

**Abstract**

A boundary integral method for the simulation of the time-dependent deformation of Newtonian or non-Newtonian drops suspended in a Newtonian fluid is developed. The boundary integral formulation for Stokes flow is used and the non-Newtonian stress is treated as a source term which yields an extra integral over the domain of the drop. The implementation of the boundary conditions is facilitated by rewriting the domain integral by means of the Gauss divergence theorem. To apply the divergence theorem smoothness assumptions are made concerning the non-Newtonian stress tensor. The correctness of these assumptions in actual simulations is checked with a numerical validation procedure. The method appears mathematically correct and the numerical algorithm is second order accurate. Besides this validation we present simulation results for a Newtonian drop and a drop consisting of an Oldroyd-B fluid. The results for Newtonian and non-Newtonian drops in two dimensions indicate that the steady state deformation is quite independent of the drop-fluid. The deformation process, however, appears to be strongly dependent on the drop-fluid. For the non-Newtonian drop a mechanical model is developed to describe the time-dependent deformation of the cylinder for small capillary numbers.

*Keywords:* Boundary integral method; Newtonian drops; Non-Newtonian drops; Slow viscous flow

* Corresponding author.



*SSDI* 0377-0257(95)01386-5

## 1. Introduction

In recent years the structure and dynamics of viscous drops has received considerable attention (for a survey see e.g. Rallison [1] and Stone [2]). The interest in this subject is mainly motivated by the desire to understand the rheology of emulsions, the mechanisms of heterogeneous mixing and the deformation of biological cells. The deformation of neutrally buoyant drops in viscous extensional flows at low Reynolds number was first studied numerically by Youngren and Acrivos [3], who modelled the drop as a capsule with an infinitely thin interface characterized by a constant interfacial tension. A boundary element method was used to perform the numerical calculations. This method has the advantage of reducing the dimension of the computational problem, which significantly reduces the computational cost. The method has extensively been used by others as well in order to simulate the behavior of drops in simple flow fields. Apart from improvements on the numerical method (Huang and Cruse [4]) recent studies have tackled more complicated flow problems (e.g. breakup of drops, Tjahjadi et al. [5]) and incorporated additional physical phenonema (e.g. the effects due to surfactants, Stone and Leal [6] and the elasticity of the membrane, Li et al. [7]).

All these studies are based on the relatively simple model in which the drop has an infinitely thin interface. A disadvantage of an infinitely thin interface is that one is forced to approximate the stresses at the interface with interfacial and (visco)elastic tensions. Another approach, taking an interface of finite thickness, has been followed by Brunn [8] and Stone and Leal [9]. Brunn [8] provides a theoretical study of a viscous particle surrounded by an elastic shell and found that the shell thickness has a significant effect on the temporal and steady state behavior of the particle. Stone and Leal [9] present a study of a drop where the finite interface consists of a viscous fluid, i.e. two concentric viscous droplets are treated numerically using the boundary integral method.

In many applications, however, the interface of the capsule consists of a non-Newtonian fluid, (e.g. lipid bilayers, Smeulders [10]). The implementation of the boundary integral method is much more complicated for these systems owing to the domain integral which arises from the non-Newtonian contributions. This implies the introduction of a grid covering the volume of the drop, next to the definition of discrete points on the boundary, and adds considerably to the numerical cost of simulations of non-Newtonian drops. However, compared to a more direct (finite difference) discretization of the Stokes equations, which would also require a grid covering the much larger region exterior to the interface, the boundary integral method for non-Newtonian drops is more efficient.

As an intermediate step towards the simulation of an actual vesicle we study in this paper a two-dimensional non-Newtonian drop in order to present and validate the extended boundary element method. In this paper we closely follow the work of Bush and co-workers [11,12], who adopted the boundary element method to analyze

extrusion experiments with non-Newtonian fluids. We extend the boundary integral method to a deforming non-Newtonian drop suspended in a Newtonian fluid. This extension is valid provided certain assumptions on the smoothness of the non-Newtonian stress tensor are satisfied. A numerical validation for a two-dimensional drop containing an Oldroyd-B fluid confirms the correctness of these assumptions. The method is further verified by comparing simulation results for Newtonian drops with results from literature. Moreover, we consider the non-Newtonian behavior of the drop and investigate the dominant relaxation times.

The organization of the paper is as follows: in Section 2 the problem is formulated. The boundary integral representation and the numerical procedure are presented in Section 3 and Section 4 respectively. Numerical results regarding the validity of the method and the influence of the (non)-Newtonian material on the deformation of the interface are discussed in Section 5. Concluding remarks concerning the applicability of the new method are given in Section 6.

## 2. Statement of the problem

The incompressible two-fluid problem considered consists of an infinitely long cylindrical membrane filled with a non-Newtonian fluid, suspended in an unbounded Newtonian fluid with viscosity $\eta^{(o)}$. The radius of the cylinder in a quiescent fluid is denoted by $a$. The Newtonian fluid is subjected to a linear flow field denoted by $\boldsymbol{u}^{\infty}$. Since the geometry is translationally invariant we can restrict the problem to a transverse section of the cylinder if we assume that there is no velocity in the $x_3$ direction (Fig. 1). In this paper we consider two types of flow; a shear flow defined by

$$u_1^{\infty} = 2Gx_2, \qquad u_2^{\infty} = 0, \tag{2.1}$$

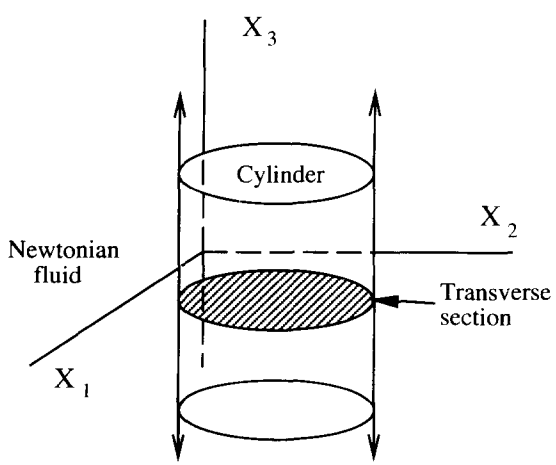


Fig. 1. Transverse section of an infinitely long (non)-Newtonian cylinder.

where $G$ is the magnitude of the flow, and an elongational flow defined by

$$u_1^{\infty} = Gx_1, \qquad u_2^{\infty} = -Gx_2. \tag{2.2}$$

The densities of the two fluids are assumed equal so there is no buoyancy in our problem. The interfacial tension acting between the two fluids is denoted by $\sigma$ and is considered to be constant along the interface $\Gamma$. In order to characterize the degree of distortion one commonly defines a deformation parameter $D$ as

$$D = \frac{L - B}{L + B}, \tag{2.3}$$

where $L$ and $B$ denote the longest and shortest lengths in the deformed state respectively. From previous analytical studies of a spherical capsule containing a Newtonian fluid (Cox [13]) it appeared that the deformation can be characterized by two parameters:

$$C = \frac{\eta^{(o)} Ga}{\sigma}, \qquad \lambda = \frac{\eta^{(i)}}{\eta^{(o)}}, \tag{2.4}$$

where $C$ is the capillary number which is a measure of the ratio between the viscous and interfacial tension stresses and $\lambda$ is the ratio between the interior and exterior viscosity. In the present case we incorporate a non-Newtonian contribution to the viscous stresses and additional parameters are needed to characterize the deformation process (De Bruijn [14]).

The domains occupied by the internal and external fluid are denoted by $\Omega^{(i)}$ and $\Omega^{(o)}$ respectively. Throughout we will work with dimensionless variables: all lengths are scaled by the undeformed capsule radius $a$, times by $1/G$, velocities by $aG$, viscosities by $\eta^{(o)}$, and tensions by $aG\eta^{(o)}$ (Li et al. [7]). Assuming that the Reynolds number ($Re = \rho a^2 G/\eta^{(o)}$, with $\rho$ the density) is small, the fluid motion may be described by the Stokes equations:

$$\partial_j \pi_{ij} = 0, \quad \forall \boldsymbol{x} \notin \Gamma \text{ and } i, j = 1, 2, \tag{2.5a}$$

$$\partial_i u_i = 0, \quad \forall \boldsymbol{x} \notin \Gamma, \tag{2.5b}$$

with $\pi_{ij}$ the Cauchy or total stress tensor and $\partial_i = \partial/\partial x_i$. In Eq. (2.5a), as in the rest of this work, the summation convention is used to indicate summation over repeated indices. The total stress tensor is given by

$$\pi_{ij} = -P\delta_{ij} + \tau_{ij}, \tag{2.6}$$

which is decomposed into a contribution from the isotropic pressure $P$ and the stress tensor $\tau_{ij}$ specified by a certain constitutive equation. The Newtonian constitutive equation for the stress tensor in the outer domain $\Omega^{(o)}$ is given by

$$\tau_{ij} = \dot{\gamma}_{ij}, \tag{2.7}$$

where $\dot{\gamma}_{ij} = \partial_i u_j + \partial_j u_i$ is the rate-of-strain tensor. In the inner domain $\Omega^{(i)}$ the stress tensor is given by a non-Newtonian constitutive equation. This stress tensor is a superposition of a 'solvent', or Newtonian part, and a 'non-Newtonian' contribution:

$$\tau_{ij} = \lambda \dot{\gamma}_{ij} + \tau_{ij}^{\mathrm{NN}}. \tag{2.8}$$

The non-Newtonian contribution typically consists of several modes:

$$\tau_{ij}^{\mathrm{NN}} = \sum_{l=1}^{n} \tau_{ij}^{(l)}, \tag{2.9}$$

where each of the $n$ modes satisfies a certain constitutive equation. The constitutive equations considered here are of the type:

$$\mathscr{D}_t \tau_{ij}^{(l)} + R_{ij}^{(l)} = 0, \tag{2.10}$$

where $\mathscr{D}_t$ is the upper-convected time derivative (Bird et al. [15]) and $R_{ij}^{(l)}$ defines the particular model adopted. The upper-convected time derivative is defined as

$$\mathscr{D}_t \tau_{ij} = \mathrm{d}_t \tau_{ij} - \partial_k u_i \tau_{kj} - \tau_{ik} \partial_k u_j, \tag{2.11}$$

with $\mathrm{d}_t \tau_{ij}$ the material time derivative which is given by

$$\mathrm{d}_t \tau_{ij} = \partial_t \tau_{ij} + u_k \partial_k \tau_{ij}, \tag{2.12}$$

with $\partial_t = \partial/\partial t$. In Section 4 we discuss the implications on the numerical scheme resulting from the differences between $\mathrm{d}_t$ and $\partial_t$, i.e. taking a Lagrangian or Eulerian description. In this paper we restrict ourselves to a non-Newtonian fluid involving a single mode given by the Maxwell model. This model finds its origin in polymer rheology and contains two parameters: a relaxation time $\mu$ and the polymer contributions to the zero-shear-rate viscosity $\eta^{(p)}$. The term $R_{ij}^{(l)}$ for the Maxwell model is given by

$$R_{ij}^{(l)} = -\frac{\lambda^{(p)}}{De} \dot{\gamma}_{ij} + \frac{1}{De} \tau_{ij}^{(l)}, \tag{2.13}$$

where we have introduced two extra dimensionless parameters:

$$De = G\mu, \qquad \lambda^{(p)} = \frac{\eta^{(p)}}{\eta^{(o)}}, \tag{2.14}$$

with $De$ the Deborah or Weissenberg number and $\lambda^{(p)}$ the ratio between the zero-shear-rate viscosity $\eta^{(p)}$ and the outer viscosity $\eta^{(o)}$.

The flow fields have to satisfy the following matching and asymptotic conditions:

$$[u_i]_\Gamma = 0, \qquad C[\pi_{ij} n_j]_\Gamma = k n_i, \tag{2.15a}$$

$$u_i = u_i^{\infty}, \quad \text{as } |\boldsymbol{x}| \to \infty, \tag{2.15b}$$

where $[\,\cdot\,]_\Gamma$ denotes the jump of the quantity between brackets across the boundary $\Gamma$, $\boldsymbol{n}$ is the outward unit normal and $k$ $(= \partial_j n_j)$ is the boundary curvature. Additionally, there is a kinematic constraint, which requires that a fluid element on the boundary $\Gamma$ remains on the boundary for all time. The kinematic constraint may be expressed by an evolution equation:

$$\mathrm{d}_t x_i = u_i, \qquad \forall \boldsymbol{x} \in \Gamma(t). \tag{2.16}$$

For both evolution equations (2.13) and (2.16) initial conditions need to be specified. For the interface $\Gamma(0)$ we start with a circular shape, whereas for the initial non-Newtonian stress contribution we assume an isotropic stress distribution (i.e. $\tau_{ij}^{\mathrm{NN}}(0) = Q\delta_{ij}$, with $Q$ an arbitrary constant).

## 3. Integral formulation of the problem

In this section we construct a solution for the velocity by means of boundary integral equations (Ladyzhenskaya [16]) assuming that the non-Newtonian stress tensor is known. The calculation of this stress tensor can be performed subsequently as is discussed in Section 4.

For the inner domain we obtain the inhomogeneous Stokes equations by substituting Eq. (2.8) in Eq. (2.5a):

$$\lambda \partial_{jj} u_i - \partial_i P = -\partial_j \tau_{ij}^{\mathrm{NN}}, \tag{3.1}$$

where we have used Eq. (2.5b). Following Ladyzhenskaya [16] we construct the solution for the velocity field in the inner domain $\Omega^{(i)}$ through:

$$\begin{aligned} c_{ik}^{(i)} u_i(\boldsymbol{x}) - \int_\Gamma K_{ijk}(\boldsymbol{r}) u_i(\boldsymbol{y}) n_j(\boldsymbol{y})\, \mathrm{d}\Gamma_y \\ = \frac{1}{\lambda} \int_{\Omega^{(i)}} J_{ik}(\boldsymbol{r}) \partial_j \tau_{ij}^{\mathrm{NN}}(\boldsymbol{y})\, \mathrm{d}\Omega_y + \frac{1}{\lambda} \int_\Gamma J_{ik}(\boldsymbol{r}) \pi_{ij}^{s}(\boldsymbol{y}) n_j(\boldsymbol{y})\, \mathrm{d}\Gamma_y, \end{aligned} \tag{3.2}$$

where $\partial_j \tau_{ij}^{\mathrm{NN}}$ is treated as a source term, $\boldsymbol{r} = \boldsymbol{x} - \boldsymbol{y}$ and $\pi_{ij}^{s} = -P\delta_{ij} + \lambda \dot{\gamma}_{ij}$. In the Newtonian case (i.e. $\tau_{ij}^{\mathrm{NN}} = 0$) Eq. (3.2) is a boundary integral representation of the velocity and hence a reduction of the dimension of the resulting problem from two to one is achieved. The non-Newtonian stress gives rise to a domain integral which makes this reduction impossible. The kernels $J_{ik}$ and $K_{ijk}$ in Eq. (3.2) are called the Green's functions for the Stokes problem. In two dimensions these kernels are given by (Ladyzhenskaya [16])

$$J_{ik}(\boldsymbol{r}) = \frac{1}{4\pi} \left\{ -\delta_{ik} \ln |\boldsymbol{r}| + \frac{r_i r_k}{|\boldsymbol{r}|^2} \right\}, \qquad K_{ijk}(\boldsymbol{r}) = -\frac{1}{\pi} \frac{r_i r_j r_k}{|\boldsymbol{r}|^4}. \tag{3.3}$$

The coefficient $c_{ik}^{(i)}$ finds its origin in the solution of the singular Stokes problem and has the following values:

$$c_{ik}^{(i)} = \begin{cases} \delta_{ik}, & \boldsymbol{x} \in \Omega^{(i)}, \\ \frac{1}{2}\delta_{ik}, & \boldsymbol{x} \in \Gamma, \\ 0, & \boldsymbol{x} \in \Omega^{(o)}, \end{cases} \tag{3.4}$$

where we have assumed that $\Gamma$ is a continuously differentiable curve. To obtain a better connection with the matching conditions (Eq. (2.15a)) it is convenient to rewrite the domain integral in Eq. (3.2) by means of the Gauss divergence theorem. The resulting expression is given by

$$c_{ik}^{(i)}u_i(\boldsymbol{x}) - \int_\Gamma K_{ijk}(\boldsymbol{r})u_i(\boldsymbol{y})n_j(\boldsymbol{y})\,\mathrm{d}\Gamma_y$$
$$= -\frac{1}{\lambda}\int_{\Omega^{(i)}} \tau_{ij}^{\mathrm{NN}}(\boldsymbol{y})\partial_j J_{ik}(\boldsymbol{r})\,\mathrm{d}\Omega_y + \frac{1}{\lambda}\int_\Gamma J_{ik}(\boldsymbol{r})\pi_{ij}(\boldsymbol{y})n_j(\boldsymbol{y})\,\mathrm{d}\Gamma_y, \tag{3.5}$$

where we have used Eqs. (2.6) and (2.8) to rewrite the last integral on the right-hand side. However, in order to apply the divergence theorem it is necessary that the non-Newtonian stress tensor is continuous and has bounded derivatives (Toose et al. [17]). For the moment we will assume that the stress tensor satisfies these conditions for all time. In Section 5.1 numerical tests are presented for an actual simulation which establish that this assumption is valid. The velocity field in the outer domain $\Omega^{(o)}$ is given by

$$c_{ik}^{(o)}u_i(\boldsymbol{x}) + \int_\Gamma K_{ijk}(\boldsymbol{r})u_i(\boldsymbol{y})n_j(\boldsymbol{y})\,\mathrm{d}\Gamma_y = u_k^{\infty}(\boldsymbol{x}) - \int_\Gamma J_{ik}(\boldsymbol{r})\pi_{ij}(\boldsymbol{y})n_j(\boldsymbol{y})\,\mathrm{d}\Gamma_y, \tag{3.6}$$

where $c_{ik}^{(o)}$ is defined by the relation

$$c_{ik}^{(i)} + c_{ik}^{(o)} = \delta_{ik}. \tag{3.7}$$

The next step is the elimination of $\pi_{ij}$ in Eqs. (3.5) and (3.6) by constructing an expression for the velocity on the boundary $\Gamma$. This is done by matching the expressions Eqs. (3.5) and (3.6) with the boundary conditions Eqs. (2.15a) and (2.15b). Performing these steps leads to

$$u_k(\boldsymbol{x}) - \frac{2(1-\lambda)}{1+\lambda}\int_\Gamma K_{ijk}(\boldsymbol{r})u_i(\boldsymbol{y})n_j(\boldsymbol{y})\,\mathrm{d}\Gamma_y = \frac{2}{1+\lambda}u_k^{\infty}(\boldsymbol{x})$$
$$-\frac{2}{(1+\lambda)}\int_{\Omega^{(i)}} \tau_{ij}^{\mathrm{NN}}(\boldsymbol{y})\partial_j J_{ik}(\boldsymbol{r})\,\mathrm{d}\Omega_y - \frac{2}{(1+\lambda)C}\int_\Gamma J_{ik}(\boldsymbol{r})n_i(\boldsymbol{y})k(\boldsymbol{y})\,\mathrm{d}\Gamma_y, \tag{3.8}$$

where we have used the fact that $c_{ik}^{(i)} = c_{ik}^{(o)} = 1/2$ for $\boldsymbol{x}\in\Gamma$. In this paper we mainly restrict to the case in which $\lambda = 1$ so Eq. (3.8) simplifies to

$$u_k(\boldsymbol{x}) = u_k^{\infty}(\boldsymbol{x}) - \int_{\Omega^{(i)}} \tau_{ij}^{\mathrm{NN}}(\boldsymbol{y})\partial_j J_{ik}(\boldsymbol{r})\,\mathrm{d}\Omega_y - \frac{1}{C}\int_\Gamma J_{ik}(\boldsymbol{r})n_i(\boldsymbol{y})k(\boldsymbol{y})\,\mathrm{d}\Gamma_y, \tag{3.9}$$

for the velocity on the interface $\Gamma$. Using Eq. (3.8) it can be shown that Eq. (3.9) is also valid in the inner and outer domains and hence the complete velocity-field can be calculated.

For the deformation of a Newtonian drop in a surrounding Newtonian fluid with different viscosity two approaches can be followed. The first approach uses Eq. (3.8) with $\tau_{ij}^{\mathrm{NN}} = 0$ leading to

$$u_k(\boldsymbol{x}) - \frac{2(1-\lambda)}{1+\lambda}\int_\Gamma K_{ijk}(\boldsymbol{r})u_i(\boldsymbol{y})n_j(\boldsymbol{y})\,\mathrm{d}\Gamma_y$$
$$= \frac{2}{1+\lambda}u_k^{\infty}(\boldsymbol{x}) - \frac{2}{(1+\lambda)C}\int_\Gamma J_{ik}(\boldsymbol{r})n_i(\boldsymbol{y})k(\boldsymbol{y})\,\mathrm{d}\Gamma_y, \tag{3.10}$$

For small values of $\lambda$ the solution of this integral equation leads to unacceptable numerical volume losses, (De Bruijn [14], Manga [18] and Tjahjadi et al. [5]). Alternatively Eq. (3.9) can be applied with $\tau_{ij}^{NN}$ equal to the difference in the stress tensor in the inner and outer domain:

$$\tau_{ij}^{NN}(\boldsymbol{y}) = (\lambda - 1)\dot{\gamma}_{ij}(\boldsymbol{y}). \tag{3.11}$$

Substitution in Eq. (3.9) leads to

$$u_k(\boldsymbol{x}) - (1-\lambda)\int_{\Omega(t)} \dot{\gamma}_{ij}(\boldsymbol{y})\partial_j J_{ik}(\boldsymbol{r})\,\mathrm{d}\Omega_y = u_k^{\infty}(\boldsymbol{x}) - \frac{1}{C}\int_{\Gamma} J_{ik}(\boldsymbol{r})n_i(\boldsymbol{y})k(\boldsymbol{y})\,\mathrm{d}\Gamma_y. \tag{3.12}$$

It can be proven that Eqs. (3.11) and (3.12) are equivalent, but Eq. (3.12) has the advantage of being less sensitive to numerical volume losses for small $\lambda$.

With these expressions we have found the solution for the velocity field in the entire flow domain, provided that the non-Newtonian stress tensor and the shape of the boundary are given. In Section 4 we will discuss the method to solve the full time-dependent problem and provide an algorithm to calculate $\tau_{ij}^{NN}$.

## 4. Numerical procedure

In this section the numerical procedure used to evaluate the boundary and domain integrals, the non-Newtonian stress tensor and the shape of the boundary $\Gamma$ are given in detail. In Section 4.1 algorithms are presented used to simulate the evolution of a non-Newtonian and Newtonian cylinder respectively. The numerical method to calculate the velocity field is described in Section 4.2. In Section 4.3 the time integration of the evolution equations (2.10) and (2.16) is presented.

### *4.1. Numerical algorithms*

The complete procedure used to simulate the evolution of the non-Newtonian cylinder can be sketched as follows. Suppose the stress tensor, $\tau_{ij}^{NN}$, the velocity field and the shape of $\Gamma$ are given at time $t$. Then we can use Eq. (2.13) to calculate the non-Newtonian stress tensor at $t + \Delta t$, whereas the new shape of the cylinder at $t + \Delta t$ can obtained using Eq. (2.16). With this new stress tensor and shape a new velocity field at time level $t + \Delta t$ can be calculated using Eq. (3.9). Repeating this explicit time integration procedure gives the evolution of the stress tensor, the velocity field and the boundary shape $\Gamma$. After some initializations (i.e. $\tau_{ij}^{NN} = Q\delta_{ij}$, the initialization of the shape of the boundary and the calculation of the initial velocity field) several steps have to be taken every time step. They are summarized in the following algorithm:

*Algorithm 4.1.: non-Newtonian fluids*

Step 1. Update the shape of the cylinder by solving Eq. (2.16) to yield $\Gamma(t+\Delta t)$.
Step 2. Calculate the stress tensor at $t+\Delta t$ by solving Eq. (2.10) given $u_i$ at time $t$.
Step 3. Calculate the velocity field at $t+\Delta t$ using Eq. (3.9) given $\tau_{ij}^{NN}$ and $\Gamma$ from step 1 and 2.

The procedure to simulate the evolution of the Newtonian cylinder differs slightly from algorithm 4.1 since Eq. (3.9) reduces to an integral equation (3.12). Use of the explicit algorithm 4.1. leads to impractically small time steps in the earlier stages. Hence, we solve Eq. (3.12) iteratively at each time step by assuming a trial velocity field. The velocity field is used to calculate $\dot{\gamma}_{ij}$ and application of Eq. (3.12) yields the new velocity field, which serves as trial velocity field in the new iteration. The iteration procedure is applied until the residual $R^{(l)}$ obtained after $l$ iterations is smaller than a prespecified small number. The residual is defined as the discrete $L_2$ norm of the difference in the velocity at the boundary $\Gamma$ of two successive iterations:

$$R^{(l)} = \left\| \boldsymbol{u}^{(l)} - \boldsymbol{u}^{(l-1)} \right\| \equiv \left\{ \frac{1}{M} \sum_{i=1}^{M} \left| \boldsymbol{u}_i^{(l)} - \boldsymbol{u}_i^{(l-1)} \right|^2 \right\}^{1/2}, \tag{4.1}$$

where $\boldsymbol{u}^{(l)}$ is the velocity on the $l$-th iteration level. To extend the region of convergence of the iterative approach the following relaxation scheme is used during the iterations:

$$\dot{\gamma}_{ij}^{(0)} = \dot{\gamma}_{ij}(t), \tag{4.2a}$$

$$\left.\begin{aligned} \dot{\gamma}_{ij}^{(l-1/2)} &= \partial_j u_i^{(l)} + \partial_i u_j^{(l)}, \\ \dot{\gamma}_{ij}^{(l)} &= \alpha \dot{\gamma}_{ij}^{(l-1)} + (1-\alpha)\dot{\gamma}_{ij}^{(l-1/2)}, \end{aligned}\right\} \quad \text{for } l \geq 1, \tag{4.2b}$$

where $u_i^{(l)}$ is the velocity field obtained with $\dot{\gamma}_{ij}^{(l-1)}$ and $\alpha$ the relaxation parameter, typically equal to 0.9. Upon convergence, after the $l^*$-th iteration, we obtain the new rate-of-strain tensor $\dot{\gamma}_{ij}(t+\Delta t) = \dot{\gamma}_{ij}^{(l^*)}$. To accelerate the convergence of the iterations we have set the initial guess for the new velocity equal to the converged velocity at the previous time step (4.2a). After some initializations (i.e. $\dot{\gamma}_{ij} = 0$, the initialization of the shape of the boundary and the calculation of the initial velocity field using the iterative method) several steps have to be taken every time step. They are summarized in the following algorithm:

*Algorithm 4.2.: Newtonian fluids*

Step a. Update the shape of the cylinder by solving Eq. (2.16) to yield $\Gamma(t+\Delta t)$.
Step b. 1. Calculation of the velocity $u_i^{(l)}$ using Eq. (3.12) given $\dot{\gamma}_{ij}^{(l-1)}$ and $\Gamma(t)$.
2. Calculation of the rate-of-strain-tensor at level $l$ using Eq. (4.2) given $u_i^{(l)}$.
3. Check for convergence and go back to 1 if necessary.
Step. c. Obtain the velocity at $t+\Delta t$ using $\dot{\gamma}_{ij}(t+\Delta t) = \dot{\gamma}_{ij}^{(l^*)}$.

It is noticed that in the limit of $\Delta t \to 0$ algorithm 4.1. is actually the same as algorithm 4.2. since the latter scheme converges in one iteration. In Sections 4.2 and 4.3 we will discuss the calculation of the velocity field and the time integration of both non-Newtonian stress tensor and boundary.

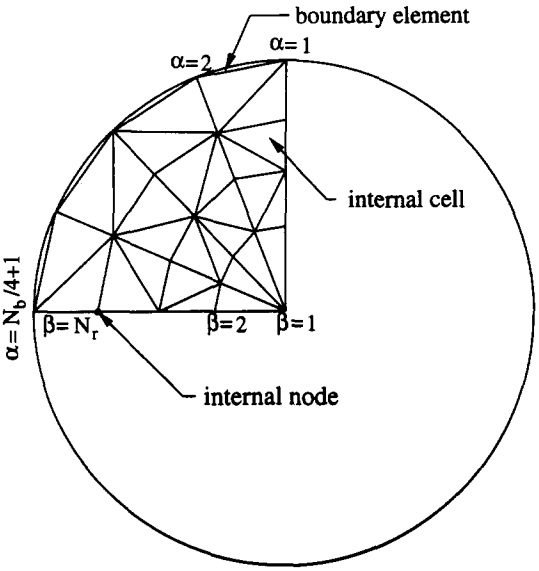


Fig. 2. The discretisation of the inner domain.

### 4.2. Evaluation of the integrals

The numerical implementation of Eqs. (3.9) or (3.12) requires the representation of the boundary $\Gamma$ into $N$ 'boundary elements' and a subdivision of the inner domain into $M$ 'internal cells'. The boundary elements used are circular arcs passing through three successive boundary points (Pozrikidis [19]). For the discretization of the inner domain we use triangles as shown in Fig. 2. The triangles in this figure result from a structured triangulation, in which the vertices have a polar distribution. Using this discretisation, Eq. (3.9) can be written as

$$u_k(\boldsymbol{x}) = u_k^{\infty}(\boldsymbol{x}) - \sum_{l=1}^{M} \int_{\Omega_l^{(r)}} \tau_{ij}^{\mathrm{NN}}(\boldsymbol{y}) \partial_j J_{ik}(\boldsymbol{r})\, \mathrm{d}\Omega - \tfrac{1}{2} \sum_{l=1}^{N} \frac{1}{C} \int_{\Gamma_l} J_{ik}(\boldsymbol{r}) n_i(\boldsymbol{y}) k(\boldsymbol{y})\, \mathrm{d}\Gamma, \tag{4.3}$$

where the factor 1/2 arises due to overlap of subsequent elements leading to a double set of boundary elements. Theoretically we could work with one set of boundary elements for the even and one for the odd numbered points. However, this approach may lead to instabilities due to odd-even decoupling, thereby resulting in severe restrictions on the maximum value of the time step. The next step is the actual numerical calculation of the integrals in Eq. (4.3). We distinguish between two cases:

(a) The boundary element or internal cell does not contain the point $\boldsymbol{x}$ (the element or cell is called regular),
(b) The boundary element or internal cell does contain the point $\boldsymbol{x}$ (the element or cell is called singular).

In case (a) the distance between a point $\boldsymbol{y}$ in the element and the point $\boldsymbol{x}$ is greater than zero, so that the singularities of the kernels lie outside the integration domain. In this case normal (Gaussian) quadrature is applied. For the boundary elements we use a 16 point Gauss–Legendre quadrature, whereas for the internal cells a 7 point modified Gauss–Legendre quadrature is used (Patridge et al. [20] and Evans [21]). In case (b) the distance between $\boldsymbol{x}$ and $\boldsymbol{y}$ can become zero and a special treatment of the singularities in the kernels is required. The logarithmic singularity in the kernel $J_{ik}(\boldsymbol{r})$ arising in the boundary integral is removed by performing the integration over the singular elements analytically. The kernel $\partial_j J_{ik}(\boldsymbol{r})$ in the domain integral contains a $1/|\boldsymbol{r}|$ singularity which can be treated by representing a triangle as (Uijttewaal et al. [22]):

$$\boldsymbol{x}(\eta,\xi) = (1-\eta)\boldsymbol{x}_1 + (\eta-\xi)\boldsymbol{x}_2 + \xi\boldsymbol{x}_3, \tag{4.4}$$

where $\boldsymbol{x}_1, \ldots, \boldsymbol{x}_3$ are the vertices of the triangle. The domain integral can be written as

$$I_k(\boldsymbol{x}) = \int_{\Omega_l^{(l)}} \{\partial_j J_{ik}(\boldsymbol{r})\}\tau_{ij}^{\mathrm{NN}}(\boldsymbol{y})\,\mathrm{d}\Omega = 2\Delta S_l \int_{\eta=0}^{1}\int_{\xi=0}^{\eta} \{\partial_j J_{ik}(\boldsymbol{r})\}\tau_{ij}^{\mathrm{NN}}(\boldsymbol{y})\,\mathrm{d}\xi\,\mathrm{d}\eta, \tag{4.5}$$

with $\Delta S_l$ the area of the $l$-th triangle. By replacing $\xi$ by $\xi = \eta\mu$ in the right-hand side of Eq. (4.5) we obtain a regular integral:

$$I_k(\boldsymbol{x}) = 2\Delta S_l \int_{\eta=0}^{1}\int_{\mu=0}^{1} \{\partial_j J_{ik}(\tilde{\boldsymbol{r}})\}\tau_{ij}^{\mathrm{NN}}(\boldsymbol{y})\,\mathrm{d}\mu\,\mathrm{d}\eta, \tag{4.6}$$

since the length of the vector $\tilde{\boldsymbol{r}}$, (defined as: $\tilde{\boldsymbol{r}} = (\boldsymbol{x}_1 - \boldsymbol{x}_2) - (\boldsymbol{x}_2 - \boldsymbol{x}_3)\mu$), is always greater than zero. The integration in Eq. (4.6) is performed analytically in the $\mu$ direction and numerically, using a 7 point Gauss–Legendre quadrature, in the $\eta$ direction.

### 4.3. Time integration

In this Section we describe a method to find the non-Newtonian stress tensor and the shape of the boundary $\Gamma$ at a new time level. Updating the shape of the cylinder requires the calculation of the positions of all the discretized points on $\Gamma$ at the new time level.

This calculation can be performed by time integration of Eq. (2.16) with an Euler forward scheme. Moving the grid points in this way leads to a clustering of both internal and boundary grid points and hence, gradually, a highly deformed grid results. The clustering arises directly from the fact that there are no restrictions on the stress tensor in tangential direction implying that the points will move freely along the boundary in the direction of the external velocity field. We can reduce this clustering by moving the boundary nodes only in the direction normal to the boundary:

$$x_i^{\alpha N_r}(t_{n+1}) = x_i^{\alpha N_r}(t_n) + \Delta t(\boldsymbol{u}^{\alpha N_r}\cdot\boldsymbol{n}^{\alpha})n_i^{\alpha}, \qquad \alpha = 1 \ldots N_b, \tag{4.7}$$

where $N_b$ is the number of points along the boundary and $N_r$ the number of points in radial direction as shown in Fig. 2. The interior grid points $\{x_i^{\alpha\beta}\}$ are found by interpolation between the center of the cylinder and the boundary points.

The new non-Newtonian stress tensor in algorithm 4.1. is obtained by integration of the constitutive equation. The upperconvected time derivative in Eq. (2.10) can be evaluated using a partial or material time derivative. The use of the partial time derivative, however, leads to a convective term which is somewhat difficult to calculate since due to the deformation of the drop a certain, fixed, point $\bar{x}$ located inside the drop at a certain time $t$ may be outside the drop at the next time level. For this problem it is more convenient to use the material time derivative which does not require an explicit calculation of the convective term. This implies that the new non-Newtonian stress tensor $\tau_{ij}^{\mathrm{NN}}$ is defined on the grid $\{\tilde{x}_i^{\alpha\beta}\}$ which is convected within the flow, i.e.

$$\tilde{x}_i^{\alpha\beta}(t_{n+1}) = \tilde{x}_i^{\alpha\beta}(t_n) + u_i^{\alpha\beta}\Delta t, \qquad \alpha = 1 \ldots N_b \text{ and } \beta = 1 \ldots N_r. \tag{4.8}$$

Since we consider only one mode in the constitutive equation we drop the superscript and replace $\tau_{ij}^{(l)}$ by $\tau_{ij}^{\mathrm{NN}}$. Integration with an Euler forward scheme leads to

$$\tau_{ij}^{\mathrm{NN}}(t_{n+1}) = \tau_{ij}^{\mathrm{NN}}(t_n) + \Delta t\{R_{ij}(t_n) - \tau_{ik}(t_n)\partial_j u_k(t_n) - \tau_{ik}(t_n)\partial_k u_j(t_n)\}, \tag{4.9}$$

where the discretized time $t_n$ is defined as $t_n = n\Delta t$ with $\Delta t$ a constant time interval. As an alternative a second- or higher-order Runga–Kutta scheme can be used. The velocity gradient $\partial_j u_k(t_n)$ in Eq. (4.9) is calculated with a finite-volume method (Van der Burg [23]). The rate-of-strain tensor in algorithm 4.2. can be calculated directly with a finite-volume method and Eq. (4.2.).

Owing to the Lagrangian approach the new stress tensor $\tau_{ij}^{\mathrm{NN}}(t_{n+1})$ resulting from Eq. (4.9) is defined on the grid $\{\tilde{x}_i^{\alpha\beta}\}$ whose positions are given by Eq. (4.8). In order to find it on the new grid $\{x_i^{\alpha\beta}\}$ the stress tensor is interpolated by

$$\tau_{ij}^{\mathrm{NN}}(\boldsymbol{x}^{\alpha\beta}) \approx \frac{1}{\Sigma 1/(d^{\alpha\beta})^2} \sum \frac{\tau_{ij}^{\mathrm{NN}}(\tilde{\boldsymbol{x}}^{\alpha\beta})}{(d^{\alpha\beta})^2}, \tag{4.10}$$

with $d^{\alpha\beta} = |\boldsymbol{x}^{\alpha\beta} - \tilde{\boldsymbol{x}}^{\alpha\beta}|$ and the summation involves points up to the nearest neighbour. To ensure that this interpolation is sufficiently accurate we introduce a time step restriction:

$$\Delta t = \epsilon \min_l \left\{ \frac{\Delta x^{(l)}}{u^{(l)}} \right\}, \tag{4.11}$$

where $\Delta x^{(l)}$ is the shortest side of the $l$-th triangle, $u^{(l)}$ the mean velocity over this triangle and $\epsilon$ is of the order 0.1.

## 5. Results and discussion

In this section we present the results of numerical calculations of the deformation of both Newtonian and non-Newtonian cylinders. In Section 5.1 we show that the

method used is mathematically correct and is second order accurate in space and time. In Section 5.2 the results for the Newtonian cylinder are compared with analytical results from literature. In Section 5.3 we study the deformation of a cylinder filled with an Oldroyd-B fluid. It is demonstrated that the inner fluid has significant effects only on the time dependent behaviour but not on the steady state deformation. The relaxation process is dominated by two characteristic times for which an approximate description at low capillary numbers is proposed.

### 5.1. *Validation of the numerical method*

The mathematical validation is based on the substitution of the numerical solution into the original equations. Suppose we have numerically solved the problem at a certain time $t$ resulting in a velocity field $\hat{u}_i(\boldsymbol{x},t)$ and non-Newtonian stress tensor $\hat{\tau}_{ij}^{\mathrm{NN}}(\boldsymbol{x},t)$. Direct substitution of the calculated fields in Eq. (3.1) is not possible since the isotropic pressure $P$ is not known. Assuming that the isotropic pressure $P$ is two times continuously differentiable within $\Omega^{(i)}$ it can be eliminated by taking the curl of Eq. (3.1). Inserting the numerically obtained solution yields

$$\lambda \partial_{ll}\{\partial_1 \hat{u}_2 - \partial_2 \hat{u}_1\} + \partial_1^2 \hat{\tau}_{12}^{\mathrm{NN}} + \partial_2^2 \hat{\tau}_{12}^{\mathrm{NN}} + \partial_1 \partial_2 \{\hat{\tau}_{22}^{\mathrm{NN}} - \hat{\tau}_{11}^{\mathrm{NN}}\} = \hat{R}(\boldsymbol{x},t), \tag{5.1}$$

where $\hat{R}(\boldsymbol{x},t)$ is the residual due to discretization errors. The discrete $L_2$-norm of this residual should asymptotically converge to zero at a specific rate as the numerically calculated quantities converge to the analytical solution in case the grid is refined. The order of accuracy can be obtained from the values of $\|\hat{R}\|$ on subsequent refinement levels from the behavior of the convergence ratio $\rho_i$, defined by

$$\rho_i = \frac{\|\hat{R}\|^{(i+1)} - \|\hat{R}\|^{(i)}}{\|\hat{R}\|^{(i+2)} - \|\hat{R}\|^{(i+1)}}, \qquad \text{for } i \geq 0, \tag{5.2}$$

where $\|\hat{R}\|^{(i)}$ is the discrete $L_2$ norm of the residual on the $i$-th refinement level. The grid is usually refined with a Romberg sequence, in which the spacing is halved at each refinement. The disadvantage of this sequence is that the computational cost is rapidly increasing. To overcome this problem we use the more efficient Bulirsch sequence (Stoer [24]):

$$h_1 = h_0/2,\ h_2 = h_0/3,\ h_{i+1} = h_{i-1}/2, \quad \text{for } i \geq 2, \tag{5.3}$$

consisting of two intertwined Romberg sequences.

For the validation we consider two different cases. In the first case the velocity $\hat{u}_i(\boldsymbol{x})$ is calculated using a given fixed stress tensor $\tau_{ij}(\boldsymbol{x})$. The components of this tensor are chosen as

$$\tau_{11} = x_1^2 x_2,\ \tau_{12} = x_1^3 + x_2^3,\ \tau_{22} = 2x_1 x_2^2.$$

Computations with a grid that is refined according to a Bulirsch-sequence show that the discrete $L_2$-norm of the residual converges to zero. The convergence rate of this residual indicates that the calculation of the velocity is second order accurate. When we take a stress tensor with components that have singular derivatives, for example

$\tau_{11} = x_1^2 x_2$, $\tau_{12} = |x_1|^{1/2} + |x_2|^{1/2}$, $\tau_{22} = 2x_1 x_2^2$,

the residual diverges. This implies that the method can detect whether the derivatives of the stress tensor are singular, which is relevant in view of the basic check on the smoothness assumptions needed to arrive at Eq. (3.5).

In the second case we consider the solution of an actual simulation after a certain number of time steps. To reduce the favorable effect of symmetry on the convergence-rate we consider a shear flow at a capillary number of 0.0265. The extra viscosity ratio $\lambda^{(p)}$ and the Deborah number *De* are 6.3 and 0.125 respectively. Both the time step and the grid are refined using a Bulirsch row. The computations were carried out using a first or a second-order accurate time-integration method. The residual, which was calculated at $t = 0.1$, converges to zero as a second-order process. Similar conclusions may be drawn at different parameters and times.

From these results we can conclude that the numerical solution satisfies the original equations and hence the smoothness assumptions made on the stress tensor are satisfied. The method has a second order spatial accuracy when the grid is refined. The accuracy in time is first order for the Euler and second order for the compact storage four stage Runga–Kutta scheme (Jameson [25]). In the next subsection it is shown that the method gives physically correct results for a Newtonian cylinder.

### *5.2. Deformation of a Newtonian cylinder*

In this Section we study the response of an infinite Newtonian cylinder in an elongational flow and compare this with results from literature. A cylinder placed in an elongational flow is known to deform until a steady state is reached if the capillary number is sufficiently low (Stone [2]). For a cylinder with $\lambda = 1$, Buckmaster and Flaherty [26] derived an expression relating the steady state deformation $\bar{D}$ to the corresponding capillary number. When it is assumed that the shape of the cylinder remains elliptical during the deformation this expression can be written as

$$C = \frac{1}{4\pi}\sqrt{(1-\bar{D})(\bar{D}+1)}\int_0^{2\pi} \frac{\bar{D}^3\cos 4\theta - 2\bar{D}^2\cos 2\theta + \bar{D}}{(1+\bar{D}^2-2\bar{D}\cos 2\theta)^{1/2}}\,\mathrm{d}\theta. \tag{5.4}$$

A numerical evaluation of this expression shows that there are two different steady state deformations for each capillary number in a certain range $0 < C < C_{\mathrm{crit}}$. The critical capillary number $C_{\mathrm{crit}}$ corresponds to the point at which the two branches coincide. Since the cylinder is not deformed when the capillary number is zero, only the "lower" branch is physically acceptable. For small $\bar{D}$, Eq. (5.4) can be expanded as

$$C = \tfrac{1}{2}\bar{D} - \tfrac{5}{8}\bar{D}^3 + O(\bar{D}^5). \tag{5.5}$$

In Fig. 3 we have drawn the lower banch of the solution of Eq. (5.4), Eq. (5.5) and some numerical results generated with algorithm 4.2. We used a grid with 96 points along the boundary. For small capillary numbers the analytical and the numerical results are in very good agreement. For larger values of $C$ the shape of the cylinder

is no longer elliptical, resulting in a small difference of about 2% between the numerical and analytical results. From our calculations we estimate that the critical capillary number is between 0.175 and 0.18. At higher capillary numbers no steady solution is obtained and the cylinder deforms until the clustering of the grid points results in the break down of our present numerical scheme. This appears consistent with the suggestion of Buckmaster and Flaherty [26] that the critical capillary number $C_{crit}$ coincides with the onset of bursting.

Richardson [27] derived the relation between the steady state deformation and the capillary number for a cylinder with $\lambda = 0$. It is given by

$$C = \frac{1}{\pi} K(\bar{D})\bar{D}, \tag{5.6}$$

where $K(\bar{D})$ is the complete elliptic integral of the first kind. For small values of $\bar{D}$, this expression can be expanded as (Byrd and Friedman [28])

$$C = \tfrac{1}{2}\bar{D} + \tfrac{1}{8}\bar{D}^3 + O(\bar{D}^5). \tag{5.7}$$

In Fig. 4 we have drawn the solutions of Eqs. (5.6) and (5.7) together with some numerical results. The numerical results were obtained using algorithm 4.2 and a grid with 96 points along the boundary and 25 points in radial direction. The results are obtained using Eq. (3.12) which gives accurate results even for $\lambda = 0$. Simulations involving the integral equation (3.10) would give rise to unacceptable numerical volume losses at $\lambda = 0$ (De Bruijn [14] and Tjahjadi [5]). From Fig. 4 we can conclude that the analytical and numerical results are in good agreement.

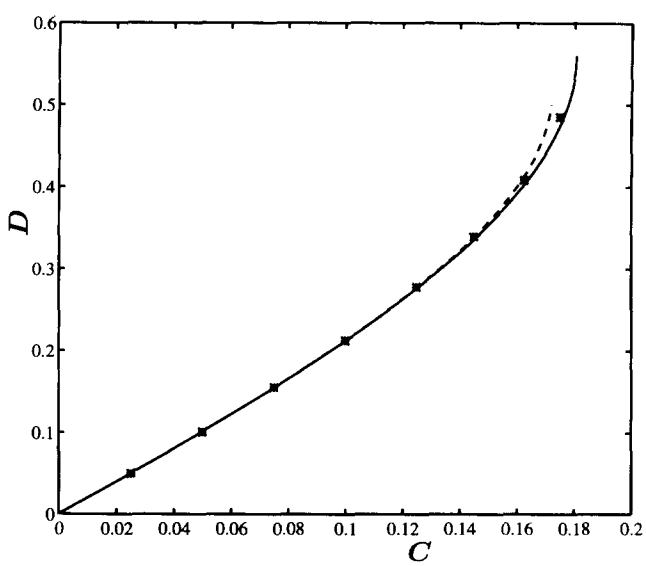


Fig. 3. Steady state deformation of a Newtonian cylinder at $\lambda = 1$ in an elongational flow. The solid and dashed curves give the solutions to Eqs. (5.4) and (5.5) respectively. The numerical results are denoted by the asterisks.

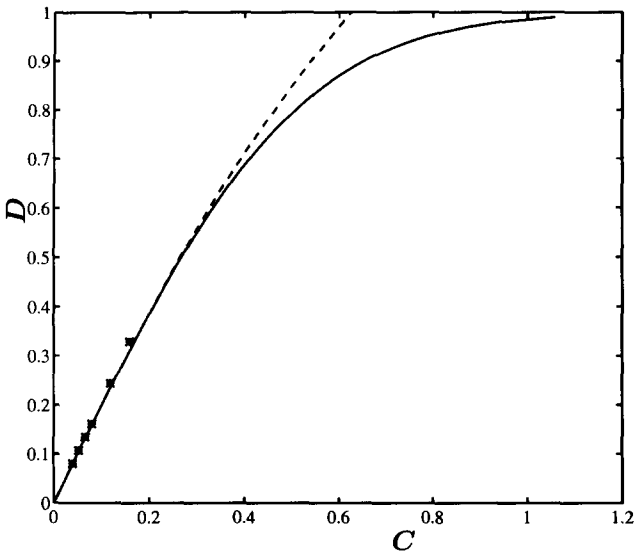


Fig. 4. Steady state deformation of a Newtonian cylinder at $\lambda = 0$ in an elongational flow. The solid and dashed curves give the solutions to Eqs. (5.6) and (5.7) respectively. The numerical results are denoted by the asterisks.

Analyzing Eq. (5.6) we observe that the deformation has an asymptote for $\bar{D} = 1$. This implies that a cylinder with $\lambda = 0$ has no critical capillary number and therefore cannot breakup. Owing to clustering of grid points for high capillary numbers we were not able to verify this limiting behavior. From Eqs. (5.5) and (5.7) we observe that in the first-order approximation, the steady state deformation is identical for $\lambda = 0$ and $\lambda = 1$. Numerical computations at other values of $\lambda$ revealed that the steady state deformation at small capillary numbers is independent of $\lambda$. This finding differs slightly from a three dimensional drop for which Taylor [29] derived that in first order approximation the $\lambda$ dependence for small $C$ is given by

$$C = \frac{1}{(\dot{\gamma}_{\max} - \dot{\gamma}_{\min})} \left( \frac{1 + \lambda}{1 + \frac{19}{16}\lambda} \right) \bar{D}, \tag{5.8}$$

where $\dot{\gamma}_{\min}$ and $\dot{\gamma}_{\max}$ are the smallest and largest principle rates-of-strain respectively. So in the three-dimensional setting there is a small variation with $\lambda$ which is absent for the cylinder.

For the time-dependent behavior of the Newtonian cylinder no analytical results are known. The results from literature for axisymmetric Newtonian drops (Cox [13], Oldroyd [30]) suggest that the deformation can be described by a first order behavior of the type:

$$D(t) = \bar{D}(1 - e^{-t/t_0}), \tag{5.9}$$

with $t_0$ the dimensionless relaxation time of the drop. This behavior closely approximates actual simulations at sufficiently low capillary numbers. For the

Newtonian cylinder the relaxation time $t_0$ can be obtained by fitting the numerical results with the function given in Eq. (5.9). The relaxation times for the cylinder obtained from a systematic set of simulations appears to be given by

$$t_0^{\mathrm{cyl}} = C(1+\lambda). \tag{5.10}$$

To verify this relation we plotted $t_0/C-1$ vs. the viscosity ratio $\lambda$ (Fig. 5). The computations were performed on a $48 \times 13$ grid and a sufficiently small time step. The results in Fig. 5 indicate that the relaxation time is indeed described by Eq. (5.10). In this figure we also plotted the analytically derived relaxation time for an axisymmetric drop (Oldroyd [30]):

$$t_0^{\mathrm{drop}} = \frac{16+19\lambda}{40(1+\lambda)}(3+2\lambda)C. \tag{5.11}$$

It can be seen that the relaxation time for the Newtonian cylinder and the axisymmetric drop differ only slightly.

From this Section we can conclude that the method gives correct results in case the stress tensor is given by a Newtonian constitutive equation. In Section 5.3 we will concentrate on a cylider which contains a non-Newtonian fluid.

### 5.3. *Deformation of a cylinder containing an Oldroyd-B fluid*

In this Section we study the response of a cylinder containing an Oldroyd-B fluid in an elongational flow. For the non-Newtonian cylinder no analytical or numerical

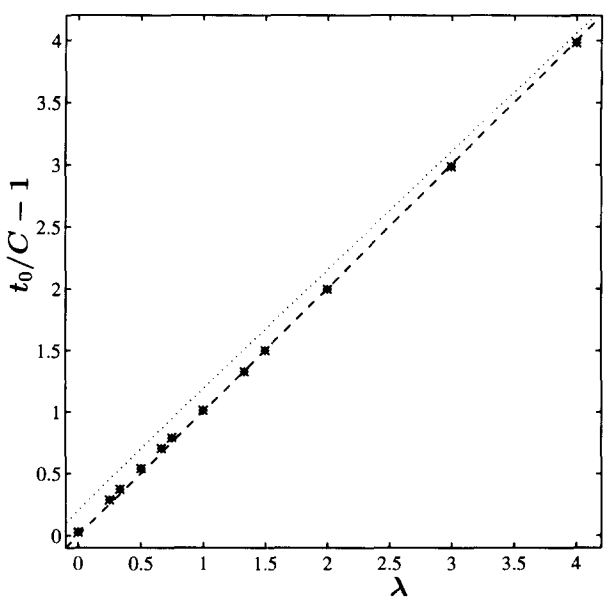


Fig. 5. The normalized relaxation time of a newtonian cylinder in an elongational flow as a function of the viscosity ratio $\lambda$. The dashed line represents equation (5.10), whereas the dotted line gives the relaxation time of an axisymmetric drop (Oldroyd [30]).

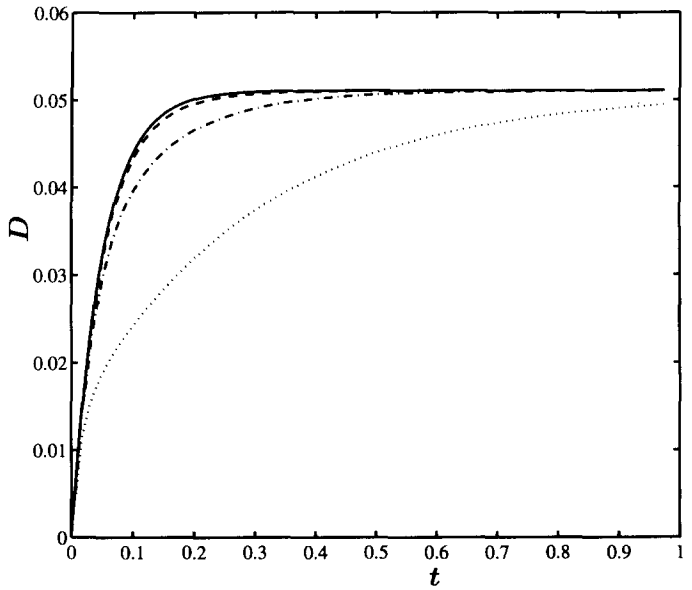


Fig. 6. Deformation of non-Newtonian cylinder in an elongational flow, ($C = 0.025$), for a fixed Deborah number ($De = 0.044$). The dotted, dash-dotted and dashed curves are the responses of a non-Newtonian cylinder with $\lambda^{(p)} = 6.6$, 0.88 and 0.118 respectively. The solid curve gives the response of the Newtonian cylinder at $\lambda = 1$.

results are known. To provide a way to verify our results we investigate several limit cases of the non-Newtonian stress tensor. Moreover it is shown that the relaxation process to a suddenly induced velocity field is dominated by two characteristic relaxation times for which an approximate model is presented. In order to remove the effects of the deformation history of the cylinder, we use the relaxed state of the non-Newtonian stress tensor at $t = 0$ (i.e. $Q = 0$). At the end of this Section we will briefly investigate the effects of a non-zero $Q$, i.e. an isotropic initial stress distribution, on the relaxation process.

The Oldroyd-B model contains three independent parameters, the viscosity ratio $\lambda$ which is chosen equal to unity, the extra viscosity ratio $\lambda^{(p)}$ and the Deborah number $De$. If either $\lambda^{(p)}$ or $De$ approaches zero an essentially Newtonian behavior should result. This fact will be used in the sequel to check the correctness of the boundary integral method for the simulation of non-Newtonian drops. In the first case $\lambda^{(p)}$ approaches zero, so the equation for the non-Newtonian stress tensor Eq. (2.10) reduces to

$$De\mathscr{D}_t\tau_{ij}^{\mathrm{NN}} + \tau_{ij}^{\mathrm{NN}} = 0,$$

where we have replaced $\tau_{ij}^{(l)}$ by $\tau_{ij}^{\mathrm{NN}}$ since only one mode is considered. This equation implies that $\tau_{ij}^{\mathrm{NN}}$ remains zero in time since $\tau_{ij}^{\mathrm{NN}} = 0$ at $t = 0$. Hence the deformation should approach the Newtonian results as $\lambda^{(p)}$ tends to zero, which is

demonstrated in Fig. 6. Here the deformation of a cylinder for several values of $\lambda^{(p)}$ and constant $De = 0.044$ is plotted. The numerical results were obtained on a $48 \times 13$ grid using a time step of 0.0015. Moreover the steady state deformation is independent of $\lambda^{(p)}$. This is similar to the Newtonian cylinder where the steady state deformation is also independent of the internal viscosity. The most important effect of variations in $\lambda^{(p)}$ is a change in the time-scale in which the steady state is reached.

In the second limit case we let $De$ approach zero, so that (2.10) reduces to

$$\tau_{ij}^{\mathrm{NN}} = \lambda^{(p)} \dot{\gamma}_{ij},$$

i.e. a Newtonian stress tensor. This implies that for $De = 0$ the non-Newtonian cylinder reduces to a Newtonian cylinder with $\lambda = 1 + \lambda^{(p)}$. The last limit we consider involves $De \to \infty$ with the magnitude of the flow kept constant. To understand and explain the behavior of the cylinder it is convenient to use a microstructural approach. In Bird et al. [31] it is shown that a microstructure consisting of linear elastic dumbbells gives the Maxwell model. It is found that the Deborah number expressed in microscopic variables is given by

$$De = G\eta^{(o)} \frac{\lambda^{(p)}}{nkT} \tag{5.12}$$

with $n$ the number of dumbbells per unit of volume, $k$ the Boltzmann constant and $T$ the temperature. It is seen that the limit $De \to \infty$ can be achieved by either taking $\lambda^{(p)} \to \infty$ or $n \to 0$. In this paper we only consider the case where the number of the dumbbells per unit of volume approaches zero. In this case the contribution of the polymer to the non-Newtonian stress also diminishes and hence the deformation should approach the Newtonian results as $De$ goes to infinity. At first sight this seems in contradiction with the definition of the Deborah number $De$. The difference can be explained by the fact that in *this* case the Deborah number alone is not a good parameter to measure the complete non-Newtonian behavior. This agrees with a remark made by Schowalter [32] (p. 213) that one should not be surprised at the inadequacy of the Deborah number to describe all of non-Newtonian fluid mechanics. In Fig. 7 the deformation of a cylinder for several values of $De$ and constant $\lambda^{(p)} = 0.9$ is plotted. The numerical results were obtained on a $48 \times 13$ grid using a time step of 0.0015. It is observed that for small $De$ the deformation of the non-Newtonian cylinder virtually coincides with the deformation of the Newtonian cylinder with $\lambda = 1 + \lambda^{(p)} = 1.9$. For large $De$ the deformation of the non-Newtonian cylinder approaches that of the Newtonian cylinder with $\lambda = 1$. From this we can conclude that the limiting behavior of the Newtonian cylinder is correctly recovered. The behavior of the non-Newtonian cylinder for moderate values of $\lambda^{(p)}$ and $De$ is surveyed next.

The results in Figs. 6 and 7 clearly demonstrate that the main effect of variations in $\lambda^{(p)}$ and $De$ is in the time dependent behavior of the cylinder. When the data of Figs. 6 and 7 are used to make a semilogarithmic plot of the normalized deformation ($D^* = 1 - D/\bar{D}$) vs. time it is observed that there are two dominant relaxation times. So, in analogy with the Newtonian cylinder, we assume that for small capillary numbers the deformation can be described by

$$D = \bar{D}\{1 - D_1 e^{-t/t_1} - D_2 e^{-t/t_2}\}, \tag{5.13}$$

where we introduced an extra relaxation time accounting for the non-Newtonian behavior. The relaxation times $t_1$ and $t_2$ can be found by fitting the deformation to the expression given in Eq. (5.13). The dependence of the relaxation time $t_1$ and $t_2$ on the parameters $\lambda^{(p)}$ and $De$ can hence be obtained from a systematic set of simulations. Before describing this dependency we will first introduce an approximate mechanical model for the rheological behavior of the non-Newtonian cylinder at low capillary numbers.

We first consider the Newtonian cylinder and observe that Eq. (5.9), which describes the deformation, can be represented by a mechanical model (Tschoegl [33]) as shown in Fig. 8. This model consists of a spring with unit spring constant parallel to two dampers with viscosities $C$ and $\lambda C$ respectively. It is noted that a damper is related to the capillary number instead of a certain viscosity which arises from the scaling of the variables used. A stress of magnitude $2C$ is applied to this model and the deformation is represented by the displacement from the unstressed state. Guided by this model, it appears natural that a non-Newtonian cylinder can be represented by a similar model in which the damper with viscosity $\lambda C$ (representing the inner fluid) is extended by a unit representing the non-Newtonian fluid. In Fig. 9 we inserted a Maxwell unit (Tschoegl [33]), consisting of a spring with spring constant $\lambda^{(p)}C/De$ in series with a damper with viscosity $\lambda^{(p)}$C. The dimensionless relaxation times $\bar{t}_1$ and $\bar{t}_2$ of this model are given by (Tschoegl [33])

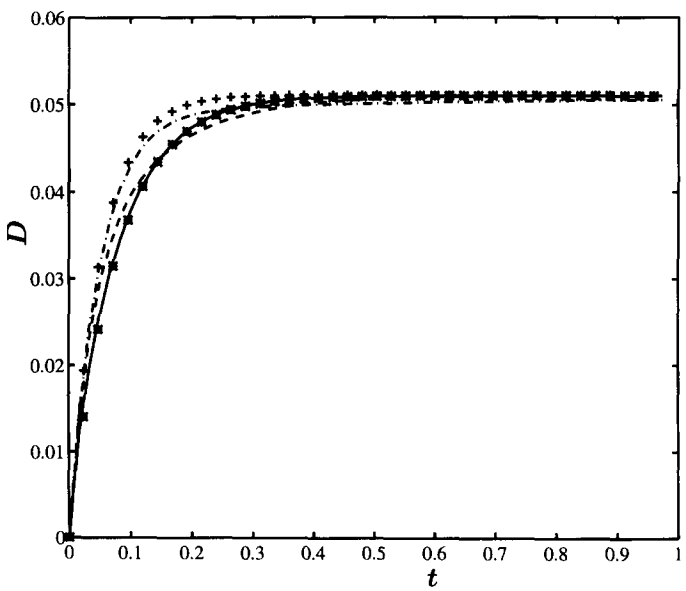


Fig. 7. Deformation of non-Newtonian cylinder in an elongational flow, ($C = 0.025$), for a fixed viscosity ratio ($\lambda^{(p)} = 0.88$). The dash-dotted, dashed and solid curves are the responses of a non-Newtonian cylinder with $De = 0.33$, 0.044 and 0.0059 respectively. The curve with the plus signs gives the response of the Newtonian cylinder at $\lambda = 1$ whereas the curve with the asterisks gives the response of the Newtonian cylinder at $\lambda = 1.88$.

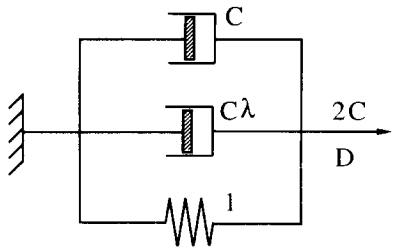


Fig. 8. Mechanical model describing the deformation of a Newtonian cylinder for small capillary numbers. In this model a stress ($2C$) is applied and the total stretch yields the deformation of the cylinder.

$$\bar{t}_{1,2} = \frac{2DeC(1+\lambda)}{De + C(1+\lambda+\lambda^{(p)}) \pm \sqrt{[De + C(1+\lambda+\lambda^{(p)})]^2 - 4DeC(1+\lambda)}}, \quad (5.14)$$

where the plus and minus signs correspond to the times $\bar{t}_1$ and $\bar{t}_2$ respectively. It is noticed that the time dependent behavior of the non-Newtonian cylinder can be described by the parameters $C$ and $\lambda$ representing the Newtonian behavior and $De$, $\lambda^{(p)}$ representing the non-Newtonian behavior. This implies that as $\lambda^{(p)}$ approaches zero, only the Newtonian behavior should remain. It is seen that $\bar{t}_1$ approaches the Newtonian limit $C(1+\lambda)$ whereas $\bar{t}_2$ approaches $De$, which is an artificial time since the non-Newtonian behavior has to disappear for $\lambda^{(p)} = 0$. For $De \to 0$ the first time $\bar{t}_1$ becomes zero and the second time $\bar{t}_2$ approaches the Newtonian limit $C(1+\lambda+\lambda^{(p)})$.

The introduced mechanical model will be compared with the Oldroyd-B cylinder by focussing on the predicted and numerically calculated relaxation times. The numerical calculations were performed on a $48 \times 13$ grid and with a sufficiently small time step. In Figs. 10 and 11 it is seen that the calculated times are in good overall agreement with the predicted times, which implies that the non-Newtonian model gives an adequate description of the deformation. The predictions for the second relaxation time appear somewhat in error at low values of $\lambda^{(p)}$ and high values of $De$. This is probably related to the unphysical limiting behavior of $\bar{t}_2$ as discussed above.

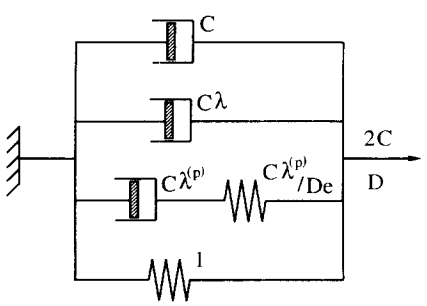


Fig. 9. Mechanical model describing the deformation of a non-Newtonian cylinder containing an Oldroyd-B fluid for small capillary numbers. In this model a stress ($2C$) is applied, whereas the total stretch yields the deformation of the cylinder.

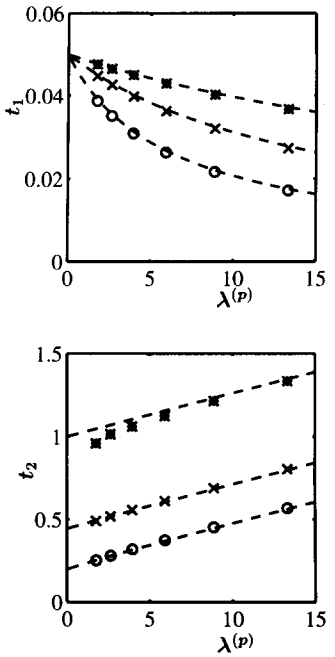


Fig. 10. Relaxation times $t_1$ and $t_2$ of a non-Newtonian cylinder with $C = 0.025$ for a set of $De$. The asterisks, crosses and circles stand for $De = 1.00$, $De = 0.44$ and $De = 0.20$ respectively. The dashed curves represent the results obtained from Eq. (5.14).

In Figs. 10 and 11 the limiting behavior described above is also clearly displayed. In Fig. 10 the Deborah number $De$ of the Oldroyd-B fluid is kept constant. It is seen that $t_1$ approaches the Newtonian limit ($\bar{t}_1 = 0.05$) as $\lambda^{(p)} \to 0$. For small values of $De$ the corresponding time $t_2$ approaches $De$. As $\lambda^{(p)} \to \infty$, $t_1$ tends to zero, whereas $t_2$ tends to infinity which corresponds to the case of a solid body. In Fig. 11 the extra viscosity ratio $\lambda^{(p)}$ is taken constant. For $De \to 0$ the first relaxation time $t_1$ becomes zero, whereas the second time approaches the Newtonian time $\bar{t}_2 = C(1 + \lambda + \lambda^{(p)})$. This is in agreement with a previous conclusion that the $De = 0$ case corresponds to a Newtonian cylinder with $\lambda = 1 + \lambda^{(p)}$. The last limit concerns $De \to \infty$ in which case $t_1$ approaches the Newtonian relaxation time at $\lambda = 1$.

From this we conclude that the introduced mechanical model (Fig. 9) gives a good description of the non-Newtonian cylinder for small capillary numbers. It is seen that the limiting behavior of the relaxation times is successfully recovered as well.

In all numerical simulations in this section the non-Newtonian stress tensor is taken zero at $t = 0$. In Fig. 12 we have plotted the response of a non-Newtonian cylinder on a suddenly induced elongational flow for several values of $Q$, i.e. using $\tau_{ij}^{NN}(0) = Q\delta_{ij}$. It is seen that the initial condition has only an effect on the time dependent behavior of the cylinder, and not on the steady state behavior. For large values of $Q$ there appears a second relaxation process at the beginning of the

deformation which is probably related to other, higher relaxation times of the non-Newtonian stress tensor.

## 6. Conclusions

In this paper we have described a boundary integral method for Newtonian and non-Newtonian drops in a viscous fluid. The non-Newtonian contribution is treated as a source term, leading to a domain integral in the boundary integral representation of the solution. To obtain a better connection with the matching conditions at the interface this domain integral is reformulated by applying Gauss' divergence theorem. In order to apply the divergence theorem the stress tensor should be sufficiently differentiable for all times. This condition was verified in actual simulations and, hence, the reformulation of the domain integral can be established. These simulations also show that the numerical method used is second order accurate.

The numerical results for the cylinder containing a Newtonian fluid have been compared with analytical results. The stationary state deformation and the critical capillary number of a Newtonian cylinder are in agreement with analytical results (Richardson [27] and Buckmaster and Flaherty [26]). It appears that the steady state deformation of both Newtonian and non-Newtonian cylinders is fairly inde-

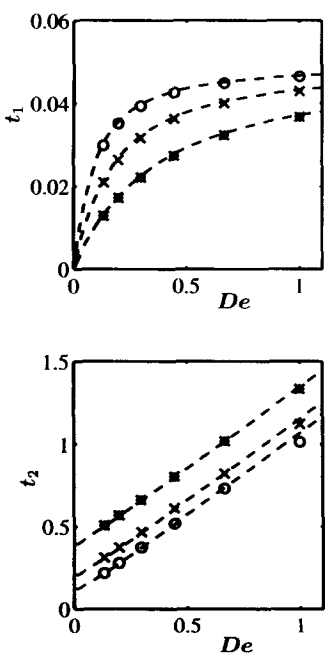


Fig. 11. Relaxation times $t_1$ and $t_2$ of a non-Newtonian cylinder with $C = 0.025$ for a set of fixed viscosity ratios. The asterisks, crosses and circles stand for $\lambda^{(p)} = 13.4$, $\lambda^{(p)} = 6.0$ and $\lambda^{(p)} = 2.6$ respectively. The dashed curves represent the results obtained from Eq. (5.14).

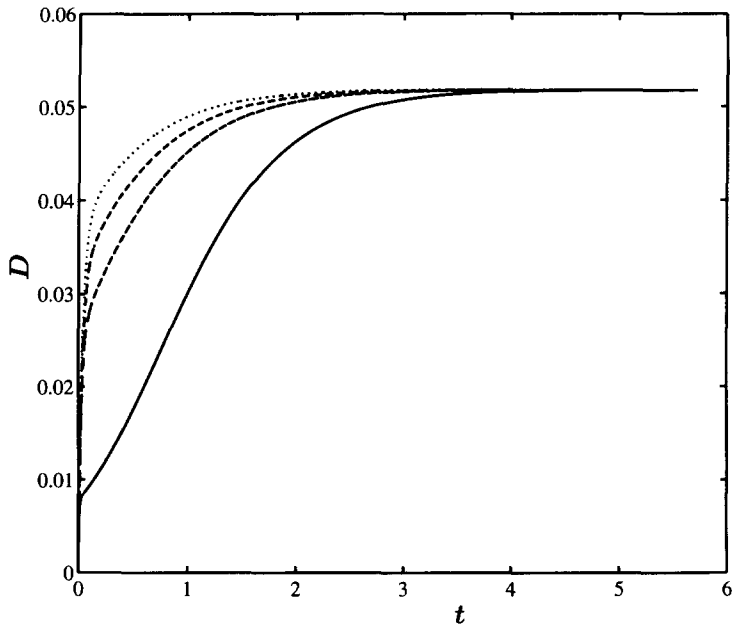


Fig. 12. Deformation of a non-Newtonian cylinder in an elongational flow, ($C = 0.025$), $\lambda^{(\varphi)} = 6.0$ and $De = 0.44$), for a set of fixed $Q$. The dotted, dash-dotted, dashed and solid curves stand for $Q = 0$, 0.4, 1.1 and 10 respectively.

pendent of the inner fluid. Analogously to the behavior of a Newtonian axisymmetric drop (Oldroyd [30]) the time dependent behavior of a Newtonian cylinder can be described with a first order model with one relaxation time. Guided by this model a new model with two relaxation times is introduced to describe the deformation of a cylinder which contains an Oldroyd-B fluid. It appears that this model gives a good description of the behavior of the cylinder for small capillary numbers.

The developed Boundary Integral method is well suited for non-Newtonian drops although computational times can be fairly long due to the domain integral that appears in the formulation. The advantage of the method lies in the fact that only the drop has to be discretized and that relatively few points are needed to give accurate results. In the near future this method will be extended to axisymmetric Newtonian drops with finitely thin non-Newtonian interfaces. In this case the advantages of the method will be fully exploited since only a thin layer has to be discretized. To improve the spatial accuracy new methods based on higher order spline interpolation are developed. Before starting with a fully three-dimensional drop the possibilities of transforming the domain integral into a boundary integral to reduce the computational time further will be studied (Zheng [34]).

## Acknowledgement

This work was supported by the J.M. Burgerscentre under EZ-project P-22. The authors wish to thank R.M.J. van Damme, H.T.M. van den Ende, Prof. J. Mellema and Prof. P.J. Zandbergen for several stimulating discussions.

## References

[1] J.M. Rallison, The deformation of small viscous drops and bubbles in shear flow, Ann. Rev. Fluid. Mech., 16 (1984) 45–66.
[2] H.A. Stone, Dynamics of drop deformation and breakup in viscous fluids, Ann. Rev. Fluid Mech., 26 (1994) 65–102.
[3] G.K. Youngren and A. Acrivos, Stokes flow past a particle of arbitrary shape: a numerical method of solution, J. Fluid Mech., 69 (1975) 377–403.
[4] Q. Huang and T.A. Cruse, Some notes on singular integral techniques in boundary element analysis, Int. J. Numer. Methods. Eng., 36 (1993) 2643–2659.
[5] M. Tjahjadi, H.A. Stone and J.M. Ottino, Satellite and subsatellite formation in capillary breakup, J. Fluid Mech., 243 (1992) 297–317.
[6] H.A. Stone and L.G. Leal, The effects of surfactants on drop deformation and breakup, J. Fluid Mech., 220 (1990) 161–186.
[7] X.Z. Li, D. Barthès-Biesel and A. Helmy, Large deformations and burst of a capsule freely suspended in an elongational flow, J. Fluid Mech., 187 (1988) 179–196.
[8] P.O. Brunn, The deformation of a viscous particle surrounded by an elastic shell in a general time-dependent flow field, J. Fluid Mech., 126 (1983) 533–544.
[9] H.A. Stone and L.G. Leal, Breakup of concentric double emulsion droplets in linear flows, J. Fluid Mech., 211 (1990) 123–156.
[10] J.B.A.F. Smeulders, The mechanical properties of lipid bylayers, Ph.D. Thesis, University of Twente at Enschede, 1992.
[11] M.B. Bush, J.F. Milthorpe and R.I. Tanner, Finite element and boundary element methods for extrusion computations, J. Non-Newtonian Fluid Mech., 16 (1984) 37–51.
[12] M.B. Bush, R.I. Tanner and N. Phan-Thien, A boundary element investigation of extrudate swell, J. Non-Newtonian Fluid Mech., 18 (1985) 143–162.
[13] R.G. Cox, The deformation of a drop in a general time-dependent fluid flow, J. Fluid Mech., 37 (1969) 601–623.
[14] R.A. De Bruijn, Deformation and breakup of drops in simple shear flow, Ph.D. Thesis, University of Eindhoven, 1989.
[15] R.B. Bird, R.C. Amstrong, O. Hassager, Dynamics of polymeric liquids: Vol. 1. fluid mechanics, Wiley-Interscience, New-York, 1987.
[16] O.A. Ladyzhenskaya, The mathematical theory of viscous incompressible flow, Gordon and Breach, New-York, 1969.
[17] E.M. Toose, R.M.J. van Damme, H.T.M. van den Ende, B.J. Geurts and J.M.G. Kuerten, A boundary element method for two-dimensional non-Newtonian drops in slow viscous flow, Memorandum No. 1221, University of Twente at Enshede, 1994.
[18] M. Manga and H.A. Stone, Buoyancy-driven interactions between two deformable viscous drops, J. Fluid Mech., 256 (1993) 647–683.
[19] C. Pozrikidis, Boundary integral and singularity methods for linearized viscous flow, Cambridge University Press, New-York, 1992.
[20] P.W. Patridge, C.A. Brebbia and L.C. Wrobel, The dual reciprocity boundary element method, Computational Mechanics Publications, Boston, 1992.
[21] G. Evans, Practical numerical integration, Wiley, Guilford, 1993

[22] S.J. Uijttewaal, E. Nijhof, R.M. Heethaar, Droplet migration, deformation, and orientation in the presence of a plane wall: A numerical study compared with analytical theories, Phys. Fluids A, 5 (1993) 819–825.
[23] J.W. Van der Burg, Numerical technique for transonic flow calculations, Ph.D. Thesis, University of Twente at Enschede, 1993.
[24] J. Stoer, Einführung in die numerische mathematic I, Springer-Verlag, Berling, 1976.
[25] A. Jameson, Transonic flow calculations, MAE-report 1651, Princeton University, 1983.
[26] J.D. Buckmaster and J.W. Flaherty, The bursting of two-dimensional drops in slow viscous flow, J. Fluid Mech., 60 (1973) 625–639.
[27] S. Richardson, Two-dimensional bubbles in slow viscous flow, J. Fluid Mech., 33 (1968) 476–493.
[28] P.F. Byrd and M.D. Friedman, Handbook of elliptic integrals for engineers and physicists, Springer-Verlag, Berlin, 1954.
[29] G.I. Taylor, The viscosity of a fluid containing small drops of another fluid. Proc. R. Soc. A., 146 (1932) 41–48.
[30] J.G. Oldroyd, The elastic and viscous properties of emulsions and suspensions. Proc. Roy. Soc. A, 218 (1953) 122–132.
[31] R.B. Bird, R.C. Amstrong, O. Hassager, Dynamics of polymeric liquids: Vol. 2. Kinetic theory, Wiley-Interscience, New-York, 1987.
[32] W.R. Schowalter, Mechanics of non-Newtonian fluids, Pergamon Press, Oxford, 1978.
[33] N.W. Tschoegl, The phenomenological theory of linear viscoelastic behaviour: an introduction, Springer-Verlag, Berlin, 1989.
[34] R. Zheng, N. Phan-Thien and C.J. Coleman, A boundary element approach for non-linear boundary-value problems, Comput. Mech., 8 (1991) 71–86.